NUCLEAR INSTRUMENTS AND METHODS 144 (1977) 129-139 ; © NORTH-HOLLAND PUBLISHING CO.

OPTIMIZATION OF ANTIPROTON FLUXES FROM TARGETS USING HADRON CASCADE CALCULATIONS

B. V. CHIRIKOV, V. A. TAYURSKI

Institute of Nuclear Physics, Novosibirsk, U.S.S.R.

H.-J. MÖHRING, J. RANFT and V. SCHIRRMEISTER

Sektion Physik, Karl-Marx-Universität, Leipzig, D.D.R.

Received 20 May 1976 and in revised form 22 February 1977

A Monte Carlo method is described for calculating particle fluxes from an extended target as a function of the occupied phase volume. The calculation is used to optimize the antiproton flux from a tungsten target by considering variation of the target dimensions and the strength of an applied magnetic field.

1. Introduction

Colliding beam facilities for e^+e^- and pp have been operating very successfully during the last years and many exciting high energy physics experiments have been completed using these machines. The application of colliding beam techniques to proton–antiproton collisions would offer new interesting possibilities for studying high energy phenomena; remember for instance the discussions with respect to particle production at large transverse momenta. A proposal of such a device was made by Budker et al. in 1970[1]).

This proposal includes a particular scheme for antiproton production by 25 GeV/c protons and gives rough estimates for the antiprotons which could be expected to be captured in the storage ring. Since this number is of crucial importance for such a project more reliable calculations and an optimization of the antiproton flux is desirable. Since the antiproton flux from an extended target is rather different from that in single hadron–hadron collisions the hadron cascade inside the target has to be considered. Much experience with hadron cascade calculations has been gained so far from other applications[2]). To increase the efficiency of capturing antiprotons the application of a suitably shaped magnetic field was proposed in ref. 1. In the cascade calculations the modification of the particle trajectories due to this magnetic field has been taken into account.

In this paper we describe some details of the calculation as well as our results.

The techniques described here might also be used for the optimization of antiproton fluxes at other energies or for the optimization of fluxes of other secondary particles.

2. Monte Carlo hadron cascade calculation

Monte Carlo hadron cascade calculations were described in detail in ref. 2 and general purpose computer programmes are available[3]). Here we are interested in the antiproton component of the hadron cascade which was not considered in refs. 2 and 3.

The straightforward inclusion of antiprotons into the methods[2,3]) would lead to a rather inefficient method for the calculation of antiproton fluxes since, according to refs. 2 and 3, complete inelastic events are sampled. Because of the small number of antiprotons produced in inelastic collisions as compared to pions and secondary nucleons a very large number of events must be sampled to be within reasonable statistical errors. Therefore we use here a modified Monte Carlo method for sampling inelastic events which allows to reduce the statistical errors of the calculated antiproton fluxes considerably. This method is similar to a method used in hadron cascade calculations before[4]).

Since many details of the hadron cascade calculations and the computer programme used correspond to the methods described in refs. 2 and 3 we describe here only the new procedure for sampling inelastic events.

We are interested in the particle flux from a target. This is an average quantity which is not influenced by fluctuations and many particle distributions in single collisions. Therefore, it is sufficient to describe the particle production processes by inclusive single particle distributions only. Likewise it is adequate to conserve energy and momentum in inelastic events only in the average over many collisions. We describe the production

of particles of kind i ($i = \mathrm{p,n},\pi^+,\pi^-,\pi^0,\bar{\mathrm{p}}$) in collisions of incoming particles of kind j on nuclei by the normalized inclusive single particle distributions

$$\frac{\mathrm{d}^3N}{\mathrm{d}^3p_i} = \hat{f}_{ij}(\boldsymbol{p}_i) = \frac{f_{ij}(\boldsymbol{p}_i)}{\int f_{ij}(\boldsymbol{p}_i)\,\mathrm{d}^3p_i}. \tag{1}$$

Details on these distributions fitted in most cases to experimental data will be given in the next section. Experimental data for several kinds of secondaries are not available, for instance neutrons or neutral pions. Therefore we use the energy sum rule as an additional constraint to ensure energy conservation in the inelastic collisions.

It has been noted that the inelasticities K_{ij}, defined as

$$K_{ij} = \frac{1}{E_{\mathrm{tot}}}\int E_i\, f_{ij}(\boldsymbol{p}_i)\,\mathrm{d}^3p_i, \tag{2}$$

are in a wide range rather independent of the total energy E_{tot} in the collision. With the K_{ij} the energy sum rule reads

$$\sum_i K_{ij} = 1. \tag{3}$$

Inelasticities K_{ij} corresponding to experimental situations are given in the next section.

Using the inelasticities K_{ij} and the average energies of particles i according to the inclusive distributions (1)

$$\langle E_{ij}\rangle = k_{i\mathrm{S}}E_{\mathrm{tot}} = \int E_i\,\hat{f}_{ij}(\boldsymbol{p}_i)\,\mathrm{d}^3p_i, \tag{4}$$

we obtain the average multiplicities for the particles i

$$n_{ij} = K_{ij}/k_{ij}, \tag{5}$$

which normalize the inclusive distributions

$$f_{ij}(\boldsymbol{p}_i) = n_{ij}\,\hat{f}_{ij}(\boldsymbol{p}_i). \tag{6}$$

The total multiplicity in the interaction of particle j with a nucleus will be

$$n_j = \sum_i n_{ij}. \tag{7}$$

Similarly to eq. (1) we introduce an arbitary normalized selection function

$$\hat{s}(\boldsymbol{p}_i) = \frac{s_{ij}(\boldsymbol{p}_i)}{\int s_{ij}(\boldsymbol{p}_i)\,\mathrm{d}^3p_i}. \tag{8}$$

This function is chosen in such a way that an efficient selection of random momenta is possible. Furthermore it should allow to enhance the production in certain regions of momentum space (for instance large transverse or longitudinal momenta, large angles, backward production etc.). Similarly as in eqs. (2)–(7) we define the quantities G_{ij}, g_j, m_{ij} and m_j:

— the inclasticities for selection

$$G_{ij} = \frac{1}{E_{\mathrm{tot}}}\int E_i\, s_{ij}(\boldsymbol{p}_i)\,\mathrm{d}^3p_i, \tag{9}$$

which can be chosen arbitrarily but should obey the sum rule

$$\sum G_{ij} = 1; \tag{10}$$

– the average energy of particle i corresponding to eq. (4)

$$g_i E_{\mathrm{tot}} = \int E_i\,\hat{s}(\boldsymbol{p}_i)\,\mathrm{d}^3p_i; \tag{11}$$

– the selection multiplicities

$$m_{ij} = G_{ij}/g_i, \tag{12}$$

$$m_j = \sum_i m_{ij}. \tag{13}$$

In our method we select only one secondary particle in each inelastic event. This particle is characterized:

- by the label i determining its kind which is selected according to the multiplicities m_{ij};
- by the momentum $\boldsymbol{p}_i$ selected from $\hat{s}(\boldsymbol{p}_i)$;
- and additionally by the weight

$$w_{ij} = \frac{\hat{f}_{ij}(\boldsymbol{p}_i)\,n_{ij}}{\hat{s}_{ij}(\boldsymbol{p}_i)\,m_{ij}/m_j} = \frac{m_j\,f_{ij}(\boldsymbol{p}_i)}{s_{ij}(\boldsymbol{p}_i)}. \tag{14}$$

3. Description of particle production

In our calculation the inclusive production of $\bar{\mathrm{p}}$, n, π^+, π^-, p and π^0 in collisions of $\bar{\mathrm{p}}$, n, π^+, π^-, and $\bar{\mathrm{p}}$ with nuclei is described by empirical formulae fitted to experimental data as far as available. Table 1 gives the formulae used and table 2 the corresponding parameters.

The expressions for p–nucleus collisions were already given in ref. 2. We are mainly interested in $\bar{\mathrm{p}}$ production and discuss, therefore, only the corresponding formula defined in a projectile–nucleon c.m.s.:

$$\frac{\mathrm{d}^2N}{\mathrm{d}p_\parallel\,\mathrm{d}p_\perp} = a_1 E_{\mathrm{cm}}^{a_2}\exp\left[-a_3\left(\frac{p_\parallel}{E_{\mathrm{cm}}}\right)^2 - a_4\,p_\perp^2\right]\times$$

$$\times\frac{p_\perp}{(p_\parallel^2+p_\perp^2+m_{\mathrm{p}}^2)^{\frac{1}{2}}}. \tag{15}$$

$p_\parallel$ denotes the c.m.s. longitudinal momentum and

TABLE 1

Empirical formulae describing inclusive particle production in proton–nucleus collisions.

$d^2N/dp_\parallel dp_\perp$ – single particle distribution in the projectile–nucleon c.m.s.;
$p_\parallel$ – c.m.s. longitudinal momentum;
$p_\perp$ – transverse momentum;
$E_{cm} = \sqrt{s}$ – c.m.s. total energy;
$y^* = \frac{1}{2}\ln[(E+p)/(E-p)]$ – c.m.s. rapidity;
$m_\perp = \sqrt{(p_\perp^2 + m_i^2)}$, m_i – mass of the particle of kind i;
a_i – parameters in particle production formulae, see table 2.

Reaction	Formula
$\left.\begin{matrix}p\\n\end{matrix}\right\} + A \to \left\{\begin{matrix}p\\n\end{matrix}\right.$	$\dfrac{d^2N}{dp_\parallel dp_\perp} = \dfrac{a_1}{E_{cm}}\left(1 + \dfrac{a_2}{E_{cm}}p_\parallel + \dfrac{a_3}{E_{cm}^2}p_\parallel^2\right) p_\perp[\exp(-a_4 p_\perp^2) + a_5\exp(-a_6 p_\perp)]$
$\left.\begin{matrix}p\\n\\\bar{p}\end{matrix}\right\} + A \to \left\{\begin{matrix}\pi^+\\\pi^0\\\pi^-\end{matrix}\right.$	$\dfrac{d^2N}{dp_\parallel dp_\perp} = \dfrac{a_1\exp\left(-\dfrac{a_2}{E_{cm}^2}p_\parallel^2\right) p_\perp[\exp(-a_3 p_\perp^2) + a_4\exp(-a_5 p_\perp)]}{(p_\parallel^2 + p_\perp^2 + m_\pi^2)^{\frac{1}{2}}}$
$\left.\begin{matrix}p\\n\end{matrix}\right\} + A \to \bar{p}$	$\dfrac{d^2N}{dp_\parallel dp_\perp} = a_1 E_{cm}^{a_2}\exp\left[-a_3\left(\dfrac{p_\parallel}{E_{cm}}\right)^2 - a_4 p_\perp^2\right]\dfrac{p_\perp}{(p_\parallel^2 + p_\perp^2 + m_p^2)^{\frac{1}{2}}}$
$\left.\begin{matrix}\pi^+\\\pi^-\end{matrix}\right\} + A \to \left\{\begin{matrix}p\\n\end{matrix}\right.$	$\dfrac{d^2N}{dp_\parallel dp_\perp} = \begin{cases}\dfrac{a_1}{E_{cm}}\left(1 + \dfrac{a_2}{E_{cm}}p_\parallel + \dfrac{a_3}{E_{cm}^2}p_\parallel^2\right) p_\perp[\exp(-a_4 p_\perp^2) + a_5\exp(-a_6 p_\perp)], & p_\parallel < 0\\ 0, & p_\parallel > 0\end{cases}$
$\left.\begin{matrix}\pi^+\\\pi^-\end{matrix}\right\} + A \to \left\{\begin{matrix}\pi^+\\\pi^0\\\pi^-\end{matrix}\right.$	$\dfrac{d^2N}{dp_\parallel dp_\perp} = \begin{cases}\left[a_5\exp\left[\left(-4\dfrac{a_6}{E_{cm}^2}p_\parallel^2\right) + a_7\right] a_8^2 p_\perp\exp(-a_8 p_\perp)\right](p_\parallel^2 + p_\perp^2 + m_\pi^2)^{\frac{1}{2}}, & p_\parallel > 0\\ \left[\left[a_1\exp\left(-4\dfrac{a_2}{E_{cm}^2}p_\parallel^2\right) + a_3\right] a_4^2 p_\perp\exp(-a_4 p_\perp)\right](p_\parallel^2 + p_\perp^2 + m_\pi^2)^{\frac{1}{2}}, & p_\parallel < 0\end{cases}$
$\left.\begin{matrix}\pi^+\\\pi^-\end{matrix}\right\} + A \to \bar{p}$	$\dfrac{d^2N}{dp_\parallel dp_\perp} = \exp\left[-a_1 m_\perp - a_2\left(\dfrac{\lvert y^*\rvert}{\frac{1}{2}\ln E_{cm}}\right)^2\right]\dfrac{p_\perp}{(p_\parallel^2 + p_\perp^2 + m_p^2)^{\frac{1}{2}}}$
$\bar{p} + A \to \left\{\begin{matrix}p\\n\end{matrix}\right.$	$\dfrac{d^2N}{dp_\parallel dp_\perp} = \begin{cases}\dfrac{a_1}{E_{cm}}\left(1 + \dfrac{a_2}{E_{cm}}p_\parallel + \dfrac{a_3}{E_{cm}^2}p_\parallel^2\right) p_\perp[\exp(-a_4 p_\perp^2) + a_5\exp(-a_6 p_\perp)], & p_\parallel < 0\\ 0, & p_\parallel > 0\end{cases}$
$\bar{p} + A \to \bar{p}$	$\dfrac{d^2N}{dp_\parallel dp_\perp} = \begin{cases}0, & p_\parallel < 0\\ \dfrac{a_1}{E_{cm}}\left(1 + \dfrac{a_2}{E_{cm}}p_\parallel + \dfrac{a_3}{E_{cm}^2}p_\parallel^2\right) p_\parallel[\exp(-a_4 p_\perp^2) + a_5\exp(-a_6 p_\perp)], & p_\parallel > 0\end{cases}$

TABLE 2

Parameters of the particle production formulae given in table 1 as determined by fits from data on different materials[2,5,6]).

Reaction	A	a_1	a_2	a_3	a_4	a_5	a_6	a_7	a_8
p, n, π^+, π^-, $\bar{p}$, $\bar{p}+A \to \bar{p}$	H	0.94	0.86	−3.37	3.78	0.47	3.6		
	Be	0.42	1.03	−3.85	5.63	3.49	2.89		
$+A \to$ p, n	Al	0.45	−1.78	0.3	5.38	3.8	2.8		
	Cu	0.44	−2.99	4.9	3.91	5.82	2.99		
	Pb	0.44	−2.99	4.9	3.91	5.82	2.99		
p, n, $\bar{p}$, $\bar{p}+A \to$	H	4.94	33.83	6.11	0.69	4.12			
	Be	1.81	33.39	3.01	5.12	7.34			
$+A \to$ π^+, π°, π^-	Al	1.54	35.54	3.7	3.03	4.94			
	Cu	2.36	37.21	5.83	0.76	3.22			
	Pb	2.36	37.21	5.83	0.76	3.22			
p, n $+A \to \pi^-$	H	2.81	44.08	5.17	0.81	4.34			
	Be	1.52	42.47	5.33	0.82	3.53			
	Al	1.54	44.62	5.67	0.83	3.17			
	Cu	1.60	46.52	6.47	0.93	3.05			
	Pb	1.60	46.52	6.47	0.93	3.05			
$\pi^+ + A \to \pi^+$	H	0.22	7.	0.	5.7	0.22	5.	0.115	5.7
$\pi^+ + A \to \pi^\circ$	H	$0.14 - \frac{0.14}{\sqrt{s}}$	13.	0.	5.7	$0.14 - \frac{0.14}{\sqrt{s}}$	9.	0.	5.7
$\pi^+ + A \to \pi^-$, $\pi^- + A \to \pi^\circ$, $\pi^- + A \to \pi^+$									
$\pi^- + A \to \pi^-$	H	0.2	13.	0.	5.7	0.2	5.	0.115	5.7
	H	10^8	7.75	85.2	4.26				
	Be	1.0×10^{-8}	7.75	85.2	4.26				
p, n $+A \to \bar{p}$	Al	1.4×10^{-8}	7.75	91.86	4.25				
	Cu	1.7×10^{-8}	5.02	94.25	3.65				
	Pb	1.4×10^{-4}	11.21	87.43	4.48				
π^+, π^- $+A \to \bar{p}$	H	8.2	2.2						

$p_\perp$ the transverse momentum of the $\bar{p}$. $E_{cm} = \sqrt{s}$ is the total c.m. energy and the parameters are given in table 2.

Experimental data concerning antiproton production are mainly available for proton–nucleus collisions at incident momenta between 19 and 24 GeV/c. The antiproton momenta measured are larger than 4 GeV/c in the laboratory frame[5,6]); in a nucleon–nucleon c.m. frame the corresponding antiprotons are going forward.

Normalized per inelastic collision the inclusive single particle distribution is nearly independent of the target material from $A = 9$ (Be) to $A = 207$ (Pb) in the momentum range experimentally known[6]). In this momentum range the ratio of inclusive distributions

$$R(p,\theta) = \frac{\mathrm{d}^2 N/\mathrm{d}p\mathrm{d}\Omega|_{\mathrm{Pb}}}{\mathrm{d}^2 N/\mathrm{d}p\mathrm{d}\Omega|_{\mathrm{Be}}} \tag{16}$$

is smaller than 1 and slightly increasing with decreasing secondary momentum.

Due to the interaction of the particles within the nucleus one expects for all kinds of secondaries that this ratio should grow further with decreasing secondary momentum and become larger than 1 at the lowest momenta.

Such a behaviour is predicted from Reggeon–parton models[7–9]) and from the energy flux cascade model[7,10]). In both kinds of models, however, the qualitative behaviour of single particle distributions as a function of the primary energy and the atomic weight A of the target nucleus dif-

fers, see fig. 1. Furthermore it is not clear whether these models can be applied without changes to $\bar{p}$-production. According to these theoretical concepts we do, however, not expect that formulae like eq. (15) which are symmetric in a nucleon–nucleon c.m.s. are correct. Otherwise there are at present no data which allow to select the correct model for production in the backward hemisphere, that is for slow antiprotons in the lab. frame. Therefore we use eq. (15) and consider this as a lower limit.

Eq. (15) was fitted only to data in a small primary energy interval, $E_0 \leqslant 24$ GeV, therefore the s-dependence obtained can not be expected to be true for higher energies. In fig. 2 we compare eq. (15) with the $\bar{p}$-production data[5,6]).

Because of the well known large deviations of antiproton distributions from Feynman scaling we use in the Monte Carlo calculation antiproton inelasticities $K_{\bar{p}j}$ changing with primary energy.

The values $K_{\bar{p}p}$ given in table 3 were obtained from pp data collected in ref. 11. Using these $\bar{p}$ inelasticities our calculations result in p multiplicities consistent with the data as shown in fig. 3.

The inelasticities for the production of all other kinds of particles are approximated by constant values in each of three energy regions, compare table 4 This discontinuous choice of the inelast-

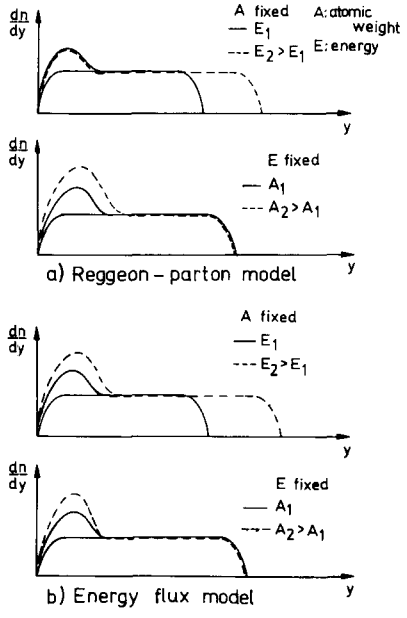

Fig. 1. Qualitative behaviour of rapidity distributions from p-nucleus collisions according to Reggeon–parton models[7–9]) and the energy flux model[7,10]).

TABLE 3

Inelasticities for antiproton production in pp collisions as determined from data collected in ref. 11.

$\sqrt{s}$	$K_{\bar{p}p}$
2.9	0.
4.5	0.00011
5.5	0.00022
6.15	0.00042
8.2	0.00071
9.	0.0011
10.	0.0014
20.	0.003
34.6	0.0042
63.4	0.008

icities causes unphysical steps in the energy dependence of particle multiplicities (not for antiprotons) which are, however, unimportant for the present application.

In our calculation we are mainly interested in good statistics for the antiproton flux. Therefore we choose for all selection inelasticities $G_{\bar{p}j}$ the value 0.5 and correspondingly reduce the G_{ij} values for other secondaries $i \neq \bar{p}$. The values used are given in table 5.

4. Particle trajectories in the magnetic field at the target

According to preliminary estimates in ref. 1 we consider the target in the form of a long thin cylinder made out of tungsten (W).

A target length of 10 cm is chosen in the first calculations corresponding to one interaction length of protons. Target radii are varied between $r_0 = 0.1$ and 0.3 cm according to technical requirements for producing strong magnetic fields in the MG range. This field is envisaged to be produced by the discharge of a capacitor through the target.

The magnetic field was calculated using a special computer programme, taking into account the dependence of electrical conductivity and heat capacity of W on temperature, neglecting, however, the melting and evaporation of the material[12]).

In typical cases the axially symmetric field can be approximated by a simple expression

$$H = H_0 \times \begin{cases} 0, & \text{for} \quad r \leqslant \frac{1}{2} r_0, \\ (2r/r_0) - 1, & \text{for} \quad \frac{1}{2} r_0 < r \leqslant r_0, \\ r_0/r, & \text{for} \quad r_0 < r, \end{cases} \tag{17}$$

TABLE 4

Inelasticities K_{ij} for the production of particles i in collisions of particles j with nuclei as used in the calculations.

$\sqrt{s}$	j \ i	p	n	π^+	π^-	$\bar{p}$	π°
<2.08	p	0.6	0.4	0.	0.	0.	0.
<2.08	n	0.4	0.6	0.	0.	0.	0.
<1.22	π^+	0.25	0.25	0.5	0.	0.	0.
<1.22	π^-	0.25	0.25	0.	0.5	0.	0.
<1.88	$\bar{p}$	0.1	0.1	0.2	0.2	0.2	0.2
$2.08<\sqrt{s}<3.76$	p	0.25	0.25	0.2	0.15	0.	0.15
$2.08<\sqrt{s}<3.76$	n	0.25	0.25	0.2	0.15	0.	0.15
$1.22<\sqrt{s}<2.96$	π^+	0.15	0.15	0.3	0.2	0.	0.2
$1.22<\sqrt{s}<2.96$	π^-	0.15	0.15	0.2	0.3	0.	0.2
$1.88<\sqrt{s}<3.76$	$\bar{p}$	0.1	0.1	0.2	0.2	0.2	0.2
>3.76	p	0.25	0.25	0.2	0.15		0.15
>3.76	n	0.25	0.25	0.2	0.15	see	0.15
>2.96	π^+	0.15	0.15	0.3	0.20	table 3[a]	0.2
>2.96	π^-	0.15	0.15	0.2	0.30		0.2
>3.76	$\bar{p}$	0.2	0.2	0.1	0.15	0.25	0.1

[a] To ensure energy conservation the small values of the $K_{\bar{p}j}$, given in table 3, are subtracted from the corresponding proton inelasticities K_{pj}.

TABLE 5

Inelasticities G_{ij} for the selection of particles as used in the cascade calculation, to calculate antiproton fluxes with high statistics.

$\sqrt{s}$	j \ i	p	n	π^+	π^-	$\bar{p}$	π°
<2.08	p	0.6	0.4	0.	0.	0.	0.
<2.08	n	0.4	0.6	0.	0.	0.	0.
<1.22	π^+	0.25	0.25	0.5	0.	0.	0.
<1.22	π^-	0.25	0.25	0.	0.5	0.	0.
<1.88	$\bar{p}$	0.062	0.062	0.125	0.125	0.5	0.125
$2.08<\sqrt{s}<3.76$	p	0.25	0.25	0.2	0.15	0.	0.15
$2.08<\sqrt{s}<3.76$	n	0.25	0.25	0.2	0.15	0.	0.15
$1.22<\sqrt{s}<2.96$	π^+	0.15	0.15	0.3	0.2	0.	0.2
$1.22<\sqrt{s}<2.96$	π^-	0.15	0.15	0.2	0.3	0.	0.2
$1.88<\sqrt{s}<3.76$	$\bar{p}$	0.062	0.62	0.125	0.125	0.5	0.125
>3.76	p	0.126	0.126	0.1	0.075	0.5	0.075
>3.76	n	0.126	0.126	0.1	0.075	0.5	0.075
>2.96	π^+	0.075	0.075	0.151	0.1	0.5	0.1
>2.96	π^-	0.075	0.075	0.1	0.151	0.5	0.1
>3.76	$\bar{p}$	0.133	0.133	0.067	0.1	0.5	0.067

where H_0 is the maximal strength at the surface of the target ($r = r_0$).

The trajectories of all charged particles of the cascade are calculated by numerical integration using the Runge–Kutta method. The step length of the integration was chosen in such a way that it did not influence the results.

If a particle leaves the target radially the trajectory is followed until the end plane of the target or – if the particle reenters — until the next in-

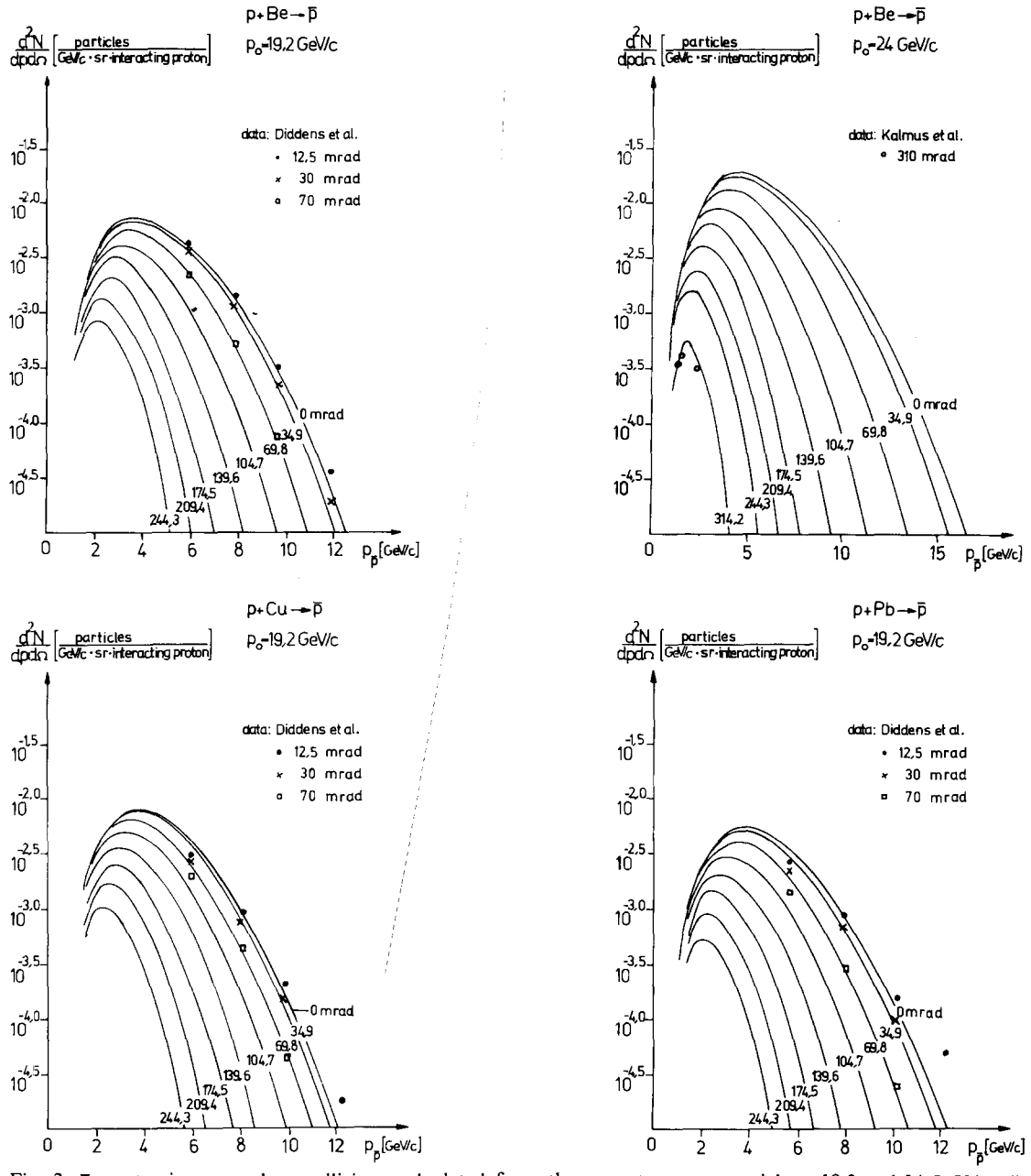

Fig. 2. p̄-spectra in p—nucleus collisions calculated from the empirical formula (15) with parameters given in table 2 compared with experimental data for p̄-production on three different target materials at 19.2 and 24 GeV/c. The curves are plotted as a function of the p̄ momentum in the laboratory frame for eight angles.

teraction. Particles moving backwards are followed until the entrance plane of the target and there considered to be lost.

5. Representation of results

All information about antiprotons crossing the end plane of the target is processed in the following way. The antiprotons are distributed into 20 momentum bins $p_i < p \leq p_{i+1}$, with $p_{i+1} = \frac{4}{3} p_i$.

The r.m.s. emittance of antiprotons is calculated in each momentum bin, computing first the average squared values $\langle x_0^2 \rangle$, $\langle y_0^2 \rangle$, $\langle \tan^2 \theta_x \rangle$, $\langle \tan^2 \theta_y \rangle$ and average correlations $\langle x_0 \tan \theta_x \rangle$, $\langle y_0 \tan \theta_y \rangle$. x_0, y_0 refer to the coordinates of the antiprotons in

the target end plane. The angles $\theta_i (i = x, y)$ are defined by $\tan\theta_i = p_i/p_z$.

According to the method described in ref. 13 the coordinates of all antiprotons are transformed to the so-called origin plane defined by requiring the correlations to vanish:

$$x = x_0 - l\tan\theta_x, \qquad y = y_0 - l\tan\theta_y. \tag{18}$$

l is the distance between the origin plane and the end plane which is calculated as

$$l = \frac{\langle x\tan\theta_x\rangle + \langle y\tan\theta_y\rangle}{\langle\tan^2\theta_x\rangle + \langle\tan^2\theta_y\rangle}. \tag{19}$$

The l-values used in eq. (18) for antiprotons in each momentum bin are calculated from the first 250 antiprotons reaching the end plane. Finally the r.m.s. emittance for each momentum bin is calculated according to

$$\phi = \tfrac{1}{2}\pi\,[(\langle x^2\rangle + \langle y^2\rangle)\,(\langle\theta_x^2\rangle + \langle\theta_y^2\rangle)]^{\frac{1}{2}}, \tag{20}$$

where the use of $\theta_{x,y}$ instead of $\tan\theta_{x,y}$ is justified by the small angles.

For each momentum bin the number of antiprotons is calculated as a function of the acceptance of the storage ring. The acceptance area of the storage ring is of elliptical shape in the phase planes

$$\frac{x^2}{x_r^2} + \frac{\theta_x^2}{\theta_{xr}^2} < 1; \qquad \frac{y^2}{y_r^2} + \frac{\theta_y^2}{\theta_{yr}^2} < 1. \tag{21}$$

The parameters x_r, y_r, $\theta_{xr,yr}$ are determined by the properties of the ring. The optimum capture of $\bar{p}$ demands the matching of the ellipses (21) to those of the beam:

$$\frac{x_r^2}{\theta_{xr}^2} = \frac{\langle x^2\rangle}{\langle\theta_x^2\rangle}; \qquad \frac{y_r^2}{\theta_{yr}^2} = \frac{\langle y^2\rangle}{\langle\theta_y^2\rangle}. \tag{22}$$

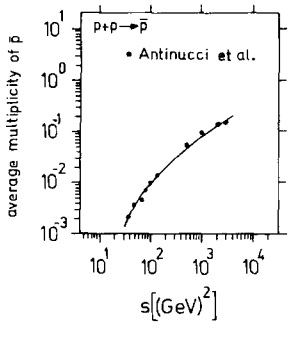

Fig. 3. Comparison of $\bar{p}$ average multiplicities $n_{\bar{p}}$ as obtained from our Monte Carlo calculation as a function of the c.m. energy with experimental data from pp collisions[11]).

At the origin plane we consider 50 acceptance ellipses with the same ratio of semi-axis equal to

$$\left[\frac{\langle x^2\rangle + \langle y^2\rangle}{\langle\theta_x^2\rangle + \langle\theta_y^2\rangle}\right]^{\frac{1}{2}}, \tag{23}$$

and with areas

$$A_n = \frac{n^2}{256}\,\phi; \qquad n = 1, 2, \ldots, 50. \tag{24}$$

In the computer programme we construct a histogram giving the number of particles in each acceptance ellipse.

6. Results

In figs. 4–11 we give the results of the calculations for a hadron cascade in tungsten targets initiated by primary protons with momentum $P_0 = 25$ GeV/c. The antiproton yield is expressed as the number of captured antiprotons per 1% $\Delta p/p$ and per incoming proton.

The primary beam has a cross section of 0.1×0.1 cm^2 and a divergence spread $-0.5 \leqslant \theta \leqslant 0.5$ mrad.

For the secondary momentum bin with the average momentum $\langle p_{\bar{p}}\rangle = 1.6$ GeV/c $(1.36 < p_{\bar{p}} \leqslant 1.81)$ our results differ only slightly from the estimates given in ref. 1. For example we obtain for this momentum bin the r.m.s. angular

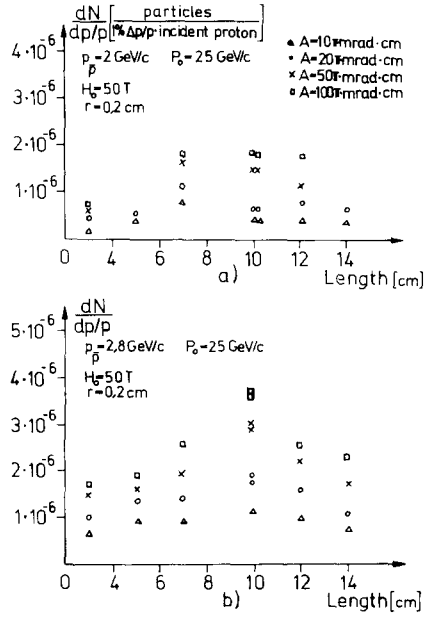

Fig. 4. Number of antiprotons captured in four different phase volumes A as a function of the target length l for fixed target radius $r = 0.2$ cm, and magnetic field $H_0 = 50$ T.

spread of the antiproton beam $\sqrt{\langle\theta^2\rangle} \approx 0.127$ rad compared to 0.15 in ref. 1. Likewise we obtain approximately the same number of captured antiprotons.

The statistical errors of the Monte Carlo method for small phase volumes are estimated to be about

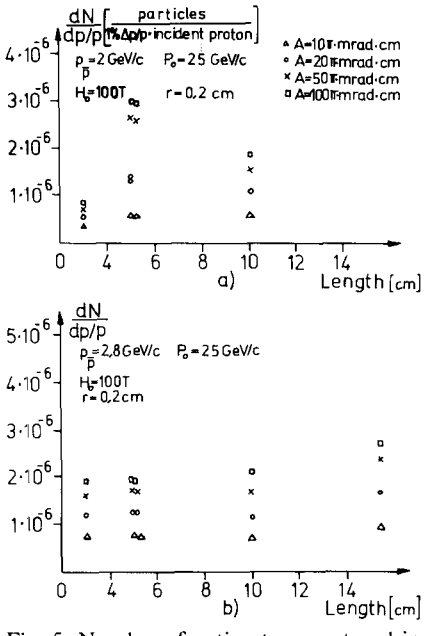

Fig. 5. Number of antiprotons captured in four different phase volumes A as a function of the target length l for fixed target radius $r = 0.2$ cm and magnetic field $H_0 = 100$ T.

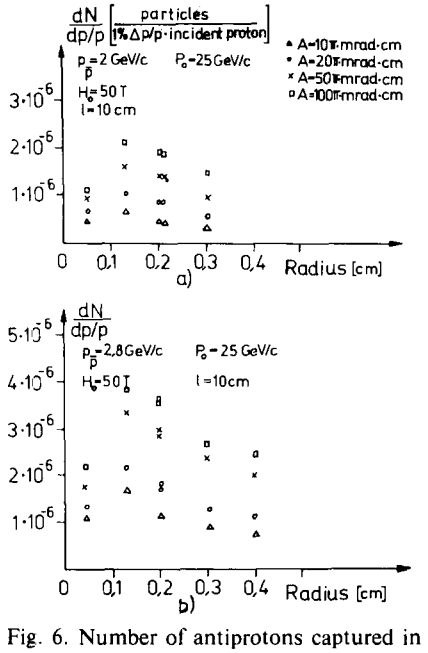

Fig. 6. Number of antiprotons captured in four different phase volumes A as a function of the target radius r for fixed target length $l = 10$ cm and magnetic field $H_0 = 50$ T.

30%. Uncertainties in the extrapolation of the particle production formulae to antiproton momenta below 4 GeV/c, where no data are available, are expected to give rise to additional systematical errors of unknown magnitude in this momentum range.

The dependence of the number of antiprotons captured in phase volumes $A = 10$, 20, 50 and 100 πmrad·cm on target lenght l, target radius r,

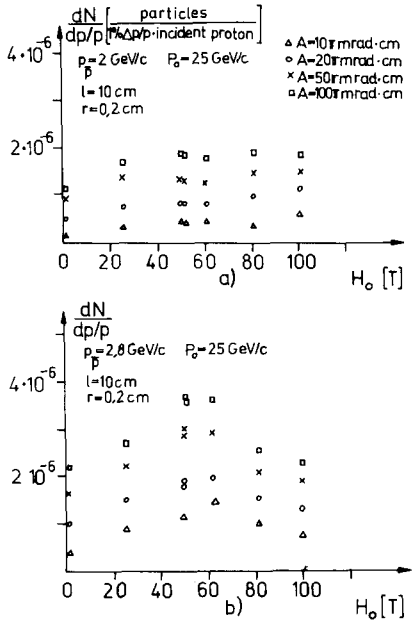

Fig. 7. Number of antiprotons captured in four different phase volumes A as a function of the magnetic field for fixed target length $l = 10$ cm and target radius $r = 0.2$ cm.

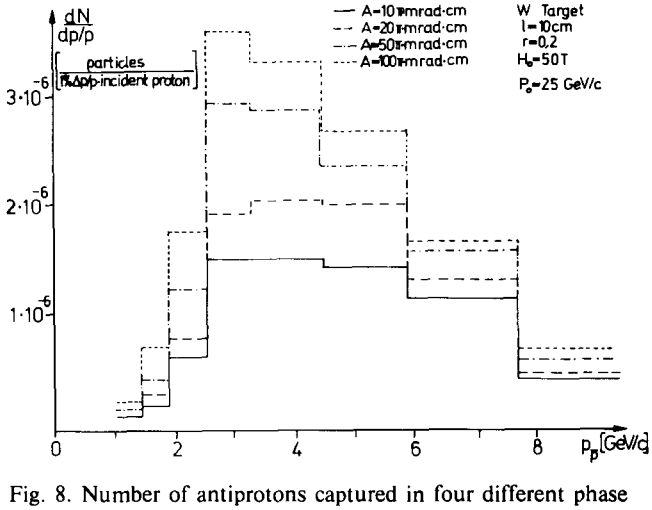

Fig. 8. Number of antiprotons captured in four different phase volumes A as a function of secondary momentum $p_{\bar{p}}$. The target parameters and primary momentum are given in the figure.

and magnetic field H_0 is given in figs. 4–7. Each set of points for the four acceptances A represents one independent cascade calculation. We show the behaviour for antiprotons within secondary momentum bins $1.81 < p_{\bar{p}} \leq 2.42$ (corresponding to $\langle p_{\bar{p}} \rangle = 2$ GeV/c) and $2.42 < p_{\bar{p}} \leq 3.22$ (corresponding to $\langle p_{\bar{p}} \rangle = 2.8$ GeV/c).

The dependence on target length l is calculated for magnetic fields $H_0 = 50$ T, see fig. 4a, b, and $H_0 = 100$ T, see fig. 5a, b. In fig. 4a and b the curves show an increasing number of captured antiprotons up to $l = 7$ cm. The broad maximum between 7 and 12 cm target length corresponds to the region of one interaction mean free path ($\lambda_{int} = 10$ cm).

In fig. 5a, b we find for the stronger magnetic field $H_0 = 100$ T only a weak dependence of the antiproton yield on the target length within the studied range ($3 \leq l \leq 15$ cm).

The antiproton flux as a function of the target radius is given in fig. 6a, b. We obtain a decreasing particle yield with increasing radius above $r = 0.15$ cm. The relatively small flux values at $r = 0.05$ cm could be understood from the effect that some primary particles miss the target.

The influence of the magnetic field H_0 is demonstrated in fig. 7a, b. With rising field we find up to $H_0 \simeq 50$ T an increase of the antiproton flux by about a factor 2. From the behaviour of the calculated points above $H_0 \simeq 50$ T we conclude that a further increase of the magnetic field strength essentially does not result in a larger antiproton yield.

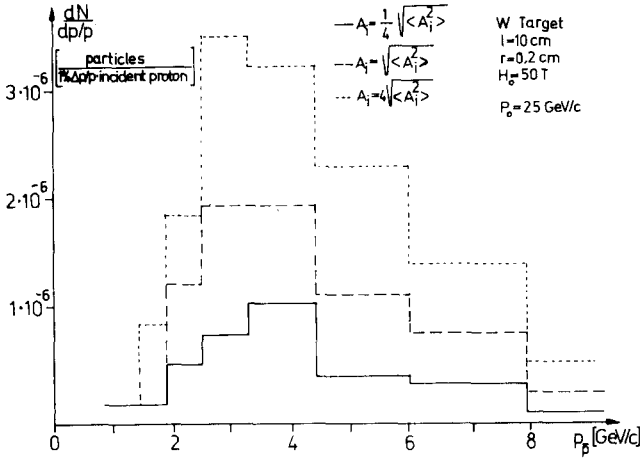

Fig. 9. Number of antiprotons captured in phase volumes $A = \frac{1}{4}\sqrt{\langle A_i^2 \rangle}$, $4\sqrt{\langle A_i^2 \rangle}$, $4\sqrt{\langle A_i^2 \rangle}$ as a function of secondary momentum p_p. $\langle A_i^2 \rangle$ is the average squared phase volume for the ith momentum bin, see fig. 10.

Figs. 8 and 9 give the number of antiprotons as functions of the secondary momentum. The particle yield captured in four different phase volumes which are constant over the whole considered momentum range is shown in fig. 8.

Fig. 9 gives for each momentum bin i the number of antiprotons captured in acceptances $A = \frac{1}{4}\sqrt{\langle A_i^2 \rangle}$, $\sqrt{\langle A_i^2 \rangle}$ and $4\sqrt{\langle A_i^2 \rangle}$ where $\langle A_i^2 \rangle$ is the average squared phase volume of the ith bin. The values for $\sqrt{\langle A_i^2 \rangle}$ as functions of the antiproton momentum $p_{\bar{p}}$ are depicted in fig. 10 and as expected they decrease with increasing secondary momentum. From figs. 8 and 9 follows that the antiproton flux captured in a larger phase volume has a higher peak at lower secondary momentum as compared to the curve for a smaller phase volume which has a flat maximum in a higher secondary momentum range.

To illustrate the effect of the primary momentum P_0 we have calculated the antiproton yield for $P_0 = 400$ GeV/c. This was done using the antiproton production formula fitted only to data with $P_0 \leq 24$ GeV/c but normalized to observed p multiplicities at higher energies. Because of the uncertainties involved in this procedure the calculation can only be considered as a rough estimate for this energy region. The number of antiprotons captured in phase volumes $A = 0.1$, 0.23, 0.5, 1 and 5 π·mrad·cm as a function of the secondary momentum $p_{\bar{p}}$ is plotted in fig. 11a for $10 < p_{\bar{p}} < 100$ GeV/c and in fig. 11b for $p_{\bar{p}} < 10$ GeV/c.

Using 400 GeV/c primary protons subtantially higher phase densities can be reached. For com-

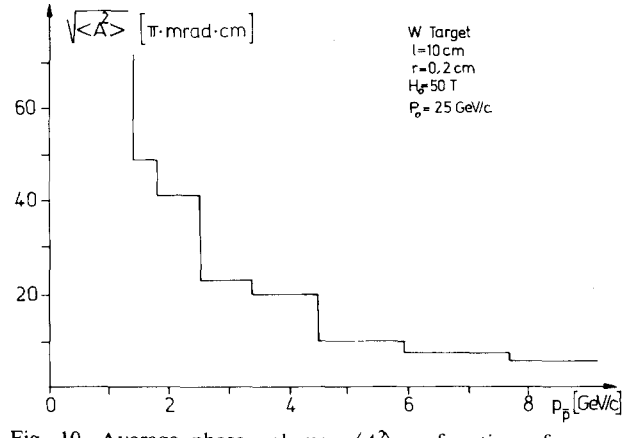

Fig. 10. Average phase volume $\sqrt{\langle A_i^2 \rangle}$ as function of secondary momentum for a particular target and primary momentum $P_0 = 25$ GeV/c.

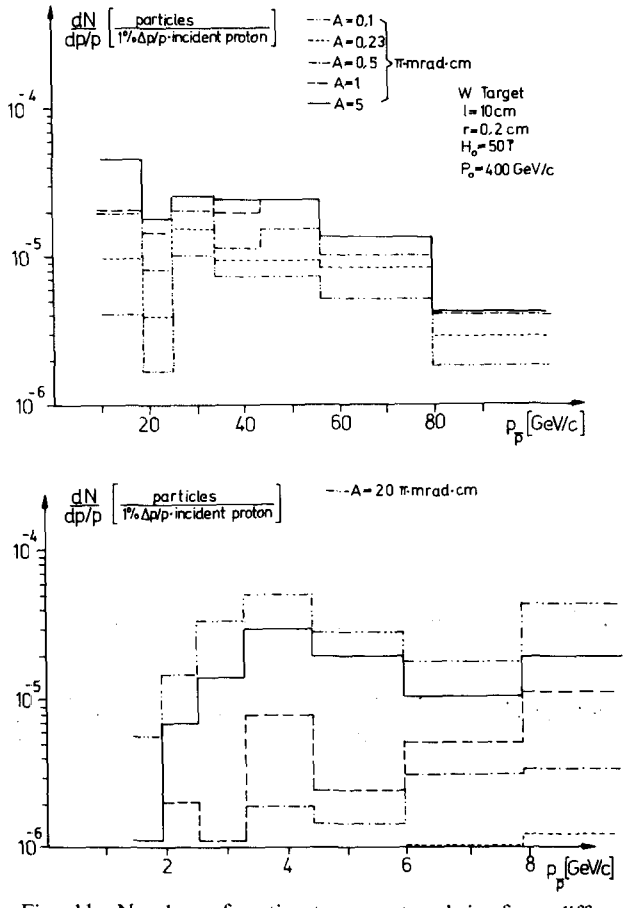

Fig. 11. Number of antiprotons captured in four different phase volumes as function of secondary momentum $p_{\bar{p}}$ for primary momentum $P_0 = 400$ GeV/c.

parable antiproton momenta and acceptances we conclude from figs. 8 and 11b that the resulting antiproton flux increases by more than one order of magnitude.

We acknowledge helpful discussions with G. Ranft, E. V. Shuryak, G. I. Silvestrov and T. A. Vsevolozhskaya and assistance with the computer programme from G. Thormann.

References

1) G. I. Budker, T. A. Vsevolozhskaya, G. I. Silvestrov and A. N. Skinsky, Proc. Sov. Nat. Particle Accelerator Conf., Moscow (1970) p. 196.
2) J. Ranft, Part. Acc. 3 (1972) 129.
3) J. Ranft and J. Routti, Computer Phys. Comm. 7 (1974) 327.
4) A. V. Ginnecken, NAL preprint (1973).
5) J. Duboc et al., CERN-Report CERN-65-2 (1965); A. N. Diddens et al., CERN-Report CERN-70-12 (1970); P. I. P. Kalmus et al., CERN-Report CERN-71-25 (1971).
6) D. Haidt, CERN-internal report TCL-Int. 71-11 (1971); M. Alston-Garnjost et al., preprint LBL-733 (1972).
7) L. Bertocchi, Trieste preprint IC/75/67 (1975).
8) O. V. Kancheli, JETP Lett. **18** (1973) 465.
9) E. S. Lehmann and G. A. Winbow, Phys. Rev. **D10** (1974) 2962.
10) K. Gottfried, Phys. Rev. Lett. **32** (1974) 957; P. M. Fishbane and J. S. Trefil, Virginia preprint (1974).
11) M. Antinucci et al., Lett. Nuovo Cim. **6** (1973) 121.
12) O. V. Zhirov, Novosibirsk report, in preparation (1974).
13) V. A. Tayursky, B. V. Chirikov and V. F. Shmakov, Novosibirsk report 64-72 (1972).